*J. Fluid Mech.* (2004), *vol.* 514, *pp.* 35–63.  
DOI: 10.1017/S0022112004009991 Printed in the United Kingdom

# Frontal geostrophic adjustment and nonlinear wave phenomena in one-dimensional rotating shallow water. Part 2. High-resolution numerical simulations

By F. BOUCHUT[1], J. LE SOMMER[2] AND V. ZEITLIN[2]†

[1]Département de Mathématiques et Applications, Ecole Normale Supérieure, France
[2]Laboratoire de Météorologie Dynamique, Ecole Normale Supérieure, France

(Received 20 May 2003 and in revised form 14 April 2004)

High-resolution shock-capturing finite-volume numerical methods are applied to investigate nonlinear geostrophic adjustment of rectilinear fronts and jets in the rotating shallow-water model. Numerical experiments for various jet/front configurations show that for localized initial conditions in the open domain an adjusted state is always attained. This is the case even when the initial potential vorticity (PV) is not positive-definite, the situation where no proof of existence of the adjusted state is available. Adjustment of the vortex, PV-bearing, part of the flow is rapid and is achieved within a couple of inertial periods. However, the PV-less low-energy quasi-inertial oscillations remain for a long time in the vicinity of the jet core. It is demonstrated that they represent a long-wave part of the initial perturbation and decay according to the standard dispersion law $\sim t^{-1/2}$. For geostrophic adjustment in a periodic domain, an exact periodic nonlinear wave solution is found to emerge spontaneously during the evolution of wave perturbations allowing us to conjecture that this solution is an attractor. In both cases of adjustment in open and periodic domains, it is shown that shock-formation is ubiquitous. It takes place immediately in the jet core and, thus, plays an important role in fully nonlinear adjustment. Although shocks dissipate energy effectively, the PV distribution is not changed owing to the passage of shocks in the case of strictly rectilinear flows.

## 1. Introduction

The present paper is the second part of the detailed investigation of the geostrophic adjustment phenomenon in the framework of the simplest possible model, the one-and-a-half dimensional rotating shallow water (1dRSW). In the companion paper (Zeitlin, Medvedev & Plougonven 2003, hereinafter referred to as Part 1), theoretical analysis of the phenomenon was undertaken. Geostrophic adjustment is a process of relaxation of an arbitrary initial configuration toward a state of geostrophic equilibrium, i.e. the equilibrium between the pressure force and the Coriolis force, via emission of inertia–gravity waves. In the 1dRSW, the geostrophic equilibria are steady states. It is worth remembering, too, that 1dRSW was used in the pioneering paper by Rossby (1938) in order to introduce the very notion of the geostrophic adjustment.

† Author to whom correspondence should be addressed: zeitlin@lmd.ens.fr

It was proved in Part 1 that a unique adjusted state exists for localized non-negative initial potential vorticity (PV) distributions if the adjustment process takes place in the open domain. It was shown that for initial configurations close enough to the geostrophic equilibrium, the adjustment is always complete (i.e. trapped wave-modes are absent), whenever the adjusted state exists. It was also shown that shock (hydraulic jump) formation happens during inertia–gravity wave propagation if the gradients of the initial height and velocity distributions are strong enough. We will sometimes loosely call this process wave-breaking in what follows. (In fact, it is an idealized model of wave-breaking which introduces dissipation in specified regions of the flow.) Shock-formation was shown to be enhanced by anticyclonic shear. Finally, the exact stationary-wave solutions were derived and analysed and were supposed to play an important role in the adjustment process in the case of periodic geometry.

The aim of the present paper is to study the influence of strongly nonlinear phenomena, especially wave-breaking, on the adjustment scenario of the jet-like disturbances. The only way to attack the strong nonlinearities is by numerical simulations and recent progress in finite-volume techniques for shallow-water flows (Audusse *et al.* 2004*a*) allows us to do this with great precision and at low cost. Below, we present the results of high-resolution shock-capturing simulations of 1dRSW adjustment. We test the semi-quantitative predictions of Part 1 and address the following problems which remain open in the case of the fully nonlinear geostrophic adjustment, namely the problems of:

(i) existence of an adjusted state in the case when PV is not positive definite;

(ii) the role of the underlying shear on wave-breaking during adjustment of frontal configurations;

(iii) the form of the relaxation law for finite-amplitude wave perturbations and its dependence of the underlying jet/front configuration;

(iv) the role of the exact periodic nonlinear-wave solutions and their interaction with shocks.

As a result, we obtain a comprehensive scenario of fully nonlinear adjustment in 1dRSW.

The plan of the paper is as follows. In § 2, we set the basic equations and briefly present the numerical method. Section 3 is dedicated to the detailed numerical study of the classical Rossby problem of adjustment of initial momentum imbalance in the open domain. In § 4, we investigate in detail the shock-formation process and test the semi-quantitative criteria for wave-breaking obtained in Part 1. Numerical analysis of the relaxation of finite-amplitude wave-packets superimposed on fronts is presented in § 5. In § 6, we consider adjustment in the periodic domain and the role of the exact nonlinear wave solutions. A brief résumé of the results obtained in each section is given at its end. We summarize the results in § 7. Numerical techniques and their inter-comparisons are described in Appendix A, and details of the numerical experiments presented in the main body of the paper are given in Appendix B.

## 2. Description of the model and the numerical procedure

Shallow-water equations on the rotating plane with no dependence on one of the coordinates ($y$) are:

$$\left.\begin{aligned} u_t + uu_x - fv + gh_x &= 0, \\ v_t + uv_x + fu &= 0, \\ h_t + uh_x + hu_x &= 0. \end{aligned}\right\} \tag{2.1}$$

Here, $u$, $v$ are the two components of the horizontal velocity, $h$ is the total fluid depth (no topographic effects will be considered), $f$ is the (constant) Coriolis parameter, $g$ is the acceleration due to gravity, and subscripts denote the corresponding partial derivatives.

The model possesses the exact steady solutions corresponding to the geostrophic equilibria:

$$fv = gh_x, \quad u = 0\,. \tag{2.2}$$

Linearization around the rest state $h = H$ gives a zero-frequency mode and inertia–gravity waves (IGW) with the standard dispersion law:

$$\omega = \pm\left(c_0^2 k^2 + f^2\right)^{1/2}\,. \tag{2.3}$$

Here, $c_0 = \sqrt{gH}$, $\omega$ is the wave-frequency and $k$ is the wavenumber. Note that the minimal frequency of IGW is $f$, the inertial frequency, and that the group velocity tends to zero for $k \to 0$.

At least for continuous fields $(h, u, v)$, each fluid particle conserves its PV:

$$q_t + uq_x = 0, \tag{2.4}$$

the PV in this context being defined as

$$q = \frac{f + v_x}{h}. \tag{2.5}$$

For states in geostrophic equilibrium, which we simply call balanced in what follows, the velocity field $v$ and the PV $q$ are completely determined by the distribution of the height-field $h$. Note that IGW bear no PV-anomaly which is defined as $q - f/H$. The absence of the PV-anomaly may be taken as the definition of the nonlinear wave-field in contradistinction with the PV-bearing vortex field. An example of initial nonlinear wave-field is an arbitrary distribution of $u$ with zero $v$ and zero $h - H$.

The model possesses an intrinsic length scale, the Rossby deformation radius $R_d = \sqrt{gH}/f$. From given velocity and length scales $U$ and $L$, respectively, the characteristic non-dimensional parameters may be constructed. They are the Rossby number $Ro = U/fL$ and the Burgers number $Bu = R_d^2/L^2$. It is easy to see that the Rossby number controls nonlinearity in (2.1), the fully nonlinear case corresponding to $Ro \sim 1$, cf. Part 1.

The motivation of our study is the accurate description of the nonlinear effects and, in particular, of the finite-time singularity (discontinuity) formation. It is therefore worth reminding ourselves of the classical framework in which the weak solutions involving discontinuities are defined.

### 2.1. *Weak solutions of the 1dRSW equations*

Equations (2.1) may be reformulated in the form of conservation laws for the two components of momentum and the mass (although momentum is not conserved because of the presence of the Coriolis acceleration in (2.1), we use the term 'conservation laws' for the equations below, as is frequently done in the literature (cf. e.g. Rozhdestvensky & Yanenko 1983); it is also known as balance law):

$$\left.\begin{aligned} &(hu)_t + \left(hu^2 + \tfrac{1}{2}gh^2\right)_x - fhv = 0,\\ &(hv)_t + (huv)_x + fhu = 0,\\ &h_t + (hu)_x = 0. \end{aligned}\right\} \tag{2.6}$$

We will be solving a Cauchy problem for these equations with a series of initial conditions prescribed in Appendix B and with either radiation or periodic boundary conditions in $x$.

Note the analogy with the (rotating) compressible gas with a specific heat ratio $\gamma = 2$, $h$ as a density variable, and the equivalent sound speed $c_0 = \sqrt{gH}$. This analogy allows us to use powerful computational methods developed in gas dynamics.

The basic properties required in order to define the *weak solutions* to (2.6) are the conservation of mass and momentum across a supposed discontinuity (see e.g. Lighthill 1978, p. 159). The weak solutions may also be obtained as solutions of a dissipative set of equations corresponding to (2.6) in the limit of vanishing viscosity (cf. e.g. Schar & Smith 1993). We use below the finite-volume numerical schemes with Riemann solvers accounting for shock formation. These schemes are, by definition, well adapted for capturing weak solutions and were extensively tested in (non-rotating) gas dynamics. The only subtle point is the treatment of the source terms introduced by the Coriolis force in (2.6).

### 2.2. *Brief overview of the numerical schemes*

Our choice of numerical procedure is motivated by the constant progress of the high-resolution shock-capturing finite-volume computation methods for the free-surface flows (cf. LeVeque 1992) and, for recent advances, Audusse *et al.* 2003. For solving the Cauchy problem we use two numerical schemes, which are presented in detail in table 1 in Appendix A. The finite-volume approach has the following advantages. On the one hand, convergence to the weak solutions is guaranteed for certain numerical flux functions. Since the set of equations (2.6) is formally equivalent to the gas dynamics equations, such numerical flux functions are known and have been extensively studied. On the other hand, the boundary conditions are well posed and are easy to maintain to the first and the second order in space. The slight inconvenience, in the context of direct comparison with Part 1, is the use of Eulerian instead of Lagrangian variables. The distinction between the slow vortical motion and rapid IGW is not automatic in Eulerian coordinates because the IGW can modify the PV field in the physical space via advection.

It should be emphasized that major improvements of the numerical codes were recently achieved with respect to the schemes used in the previous numerical studies of 1dRSW adjustment by Kuo & Polvani (1997, 1999). First, the methods we use below have been designed with special care as to the computation of the source terms due to the Coriolis forcing. An *ad hoc* discretization of these terms is made in Method 1 (cf. LeVeque 1998) whereas they are incorporated in the relaxation hyperbolic solver in Method 2 (cf. Audusse *et al.* 2004*a*). The result of these improvements is that both methods are less diffusive than the standard operator-splitting methods and they can resolve the near-equilibrium states well since they conserve exactly the steady states. Secondly, the hyperbolic solver of Method 2 intrinsically satisfies the entropy condition; this is not guaranteed by the classical Roe solver. The practical effect of this improvement is that it allows us to avoid over-diffusive corrections applied to correct the Roe solver (cf. LeVeque 1992). Finally, this solver allows the computation of the dry-bed, a situation which may occur when $h \to 0$ (see below, and also Audusse, Bristeau & Perthame 2004*b* for extended tests).

The basic properties of the numerical schemes are summarized in table 1 in Appendix A, and a complete description of both methods is given there. For each of the numerical experiments described below, we give the exact formulation of the

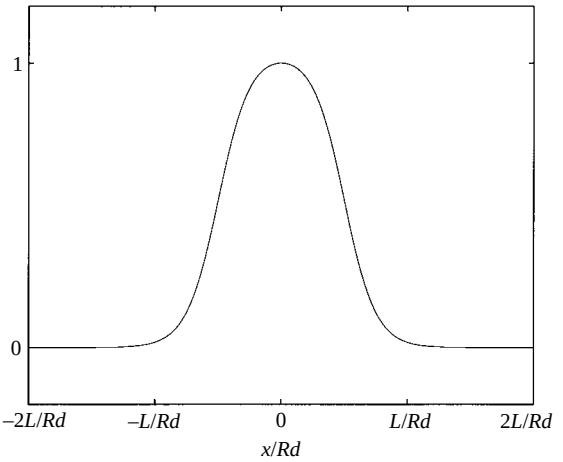


FIGURE 1. The normalized profile $N_L(x)$ used in the numerical simulations, cf. Appendix B.

initial conditions, as well as all relevant parameters in Appendix B. The superscripts $a, b, \ldots$ in the parameters correspond to experiments $a$, $b$, etc. respectively.

## 3. Rossby adjustment in the open domain

We start our study by adjustment of unbalanced jets, the classical Rossby problem being the prototype.

### 3.1. *The classical Rossby problem*

Experiment $a$ (cf. Appendix B) illustrates the evolution of a simple jet-shaped initial momentum imbalance which consists in a localized $v$-velocity distribution superimposed on the rest state.

The shape of the velocity profile of the jet $v(x)$ is plotted in figure 1, the same normalized profile

$$N_L(x) = \frac{(1+\tanh(4x/L+2))\,(1-\tanh(4x/L-2))}{(1+\tanh(2))^2} \tag{3.1}$$

is also used in other experiments. The dimensional parameters $g$, $H$, $f$ are fixed once for all simulations. Additional parameters $V$, $L$ – the maximum zonal velocity and the width of the jet – are defined for experiment $a$. The initial conditions and resulting dynamics depend on two non-dimensional parameters: the Rossby number $Ro^a$ and the Burgers number $Bu^a$. As was already mentioned, the fully nonlinear adjustment corresponds to $Ro^a \sim 1$. A natural time scale is $T_f = 2\pi/f$.

The evolution of the height field $h(x,t)$ is shown in figure 2 for $Ro^a = 1$ and $Bu^a = 0.25$. As expected, the height field adjusts to the momentum imbalance by emitting IGW which propagate out from the jet. As seen in figure 2, two discontinuities form very rapidly at the wavefront. The formation of shocks in RSW (i.e. the fact that rotation does not inhibit wave-breaking) was previously predicted by Houghton (1969) and observed by Kuo & Polvani (1997) in their numerical study of the rotating dam-break problem. The semi-quantitative theory of shocks in 1dRSW was given in Part 1. By analysing a variety of jet parameters, we plot the statistics of shocks formation in figure 3. This figure shows that shock formation is ubiquitous for large enough Rossby numbers. It should be stressed that breaking happens rapidly at

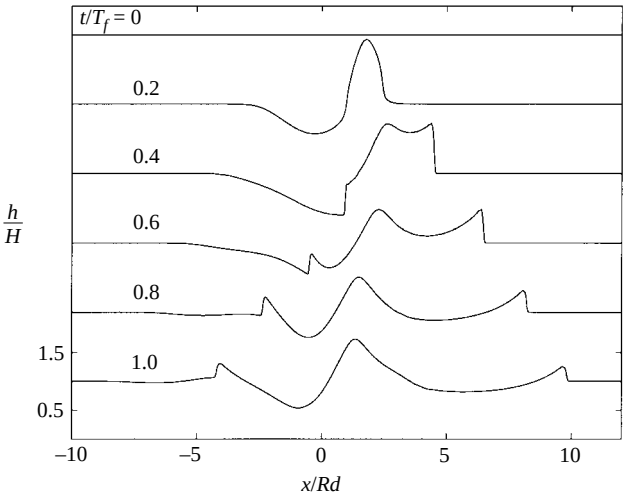


FIGURE 2. Snapshots of the Rossby adjustment, experiment *a*. Two shocks are formed at $t = 0.3$ and propagate to the left and to the right from the jet, respectively. One of the shocks is formed immediately within the jet core. *h*, height; $Ro = 1$; $Bu = 0.25$.

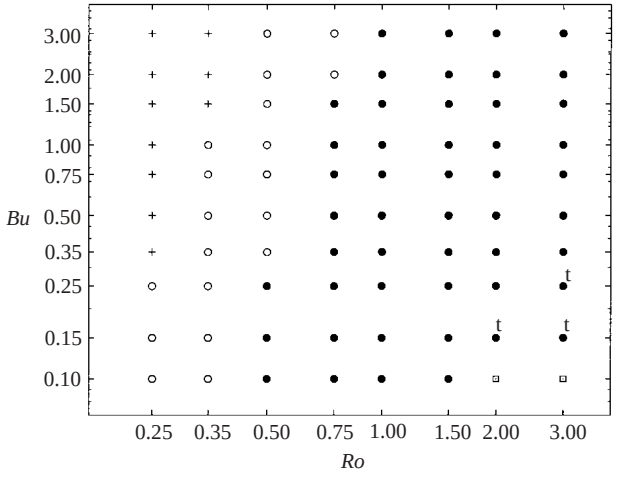


FIGURE 3. Statistics of the shock formation in the Rossby adjustment problem on the $Bu^a - Ro^a$ plane: each point corresponds to a run with the corresponding parameters $Bu^a$ and $Ro^a$. ●, breaking happens in $t < \pi/f$; ○, breaking event in $\pi/f < t < 2\pi/f$; +, breaking in $t > 2\pi/f$. Appearance of transonic shocks, i.e. those with propagation velocity changing sign during evolution, are marked by the superscript $t$. □, drying was observed for large $Ro^a$ and small $Bu^a$.

$t \sim \pi/f$, and immediately within the jet core. Hence, the breaking phenomenon can, in principle, modify the background flow as it necessarily involves dissipative processes. The effect of breaking upon the background flow is studied in detail in § 4. It should be noted that shock-formation in the present case of strong initial imbalance first happens at the anticyclonic side of the jet in accord with the qualitative criteria of Part 1.

The vortical PV-bearing part of the flow reached an equilibrium state for all parameter values we studied. This equilibrium state is basically geostrophic, as

illustrated in figure 4. The adjustment of the vortical flow is rapid, it happens in several inertial periods.

The equilibrium is achieved even if the initial potential vorticity is not positive-definite. This is illustrated in figure 5 and was not predicted by the analytical study in Part 1. Furthermore, a considerable advective shift of the potential vorticity takes place on route to the geostrophic state. This finite-amplitude effect is a recoil due to the IGW emission. Finally, as was first noticed by Kuo & Polvani (1997) in their numerical simulations, some (PV-less) oscillations with frequencies close to $f$ remain for a long time in the vicinity of the jet (cf. figures 4 and 13). The precise nature of these oscillations will be determined in § 5.

### 3.2. *The double-jet configuration*

In order to extend the investigation beyond the single-jet geometry of the momentum imbalance, especially concerning the existence of the adjusted state for negative initial PVs, we repeated the experiment for the case of initial double-jet configuration (experiment *b*, cf. Appendix C). The definition of the initial state now requires three independent parameters: the Rossby number $Ro^b$, the Burgers number $Bu^b$ and an additional parameter which fixes the distance between the maxima of the jets, $\alpha^b$. There exist two different classes of initial states depending on the sign of $\alpha^b$, as illustrated in figure 6. In both cases, the flow evolution goes through the same stages as in the single-jet case, as to the shock formation and the geostrophic equilibrium in the final state. The initial versus final PV-fields are plotted in figure 7. Note that in the case $\alpha^b = -1$ (positive mass anomaly of the end-state) the PV distribution shrinks, whereas in the case $\alpha^b = 1$ (negative mass anomaly of the end-state) the PV distribution stretches. Note also that the amplitude of the advective shift is now smaller than in the previous case.

### 3.3. *Summary of the Rossby adjustment results*

(i) Adjusted state is reached even for non positive-definite PVs after a rapid stage of IGW emission;

(ii) for a wide range of parameters, IGW break within or close to the jet core;

(iii) quasi-inertial oscillations remain in the jet region for long times.

Below we will study in more detail the wave-breaking phenomenon and the properties of the observed quasi-inertial oscillations.

## 4. Shock formation

In this section we study shock formation and test the qualitative criteria for wave breaking found in Part 1. Before proceeding, we briefly recall the classical hydraulic theory in order to explain why, although energy is dissipated in shocks, this dissipation does not affect the PV-conservation.

### 4.1. *Reminder of the hydraulic theory*

The analogy between the shallow-water equations and the compressible Euler equations is well known. It gives a mathematically rigorous framework to describe the hydraulic jumps as gas dynamics shock waves (see Lighthill 1978). The standard discontinuity calculus holds for 1dRSW, as well. (For non-rotating case see Whitham 1974; for rotating case see Pratt 1983, 1984 and Nof 1984). Weak solutions are known to be completely determined if the Rankine–Hugoniot (RH) conditions are specified together with the entropy condition. In our case,the RH conditions

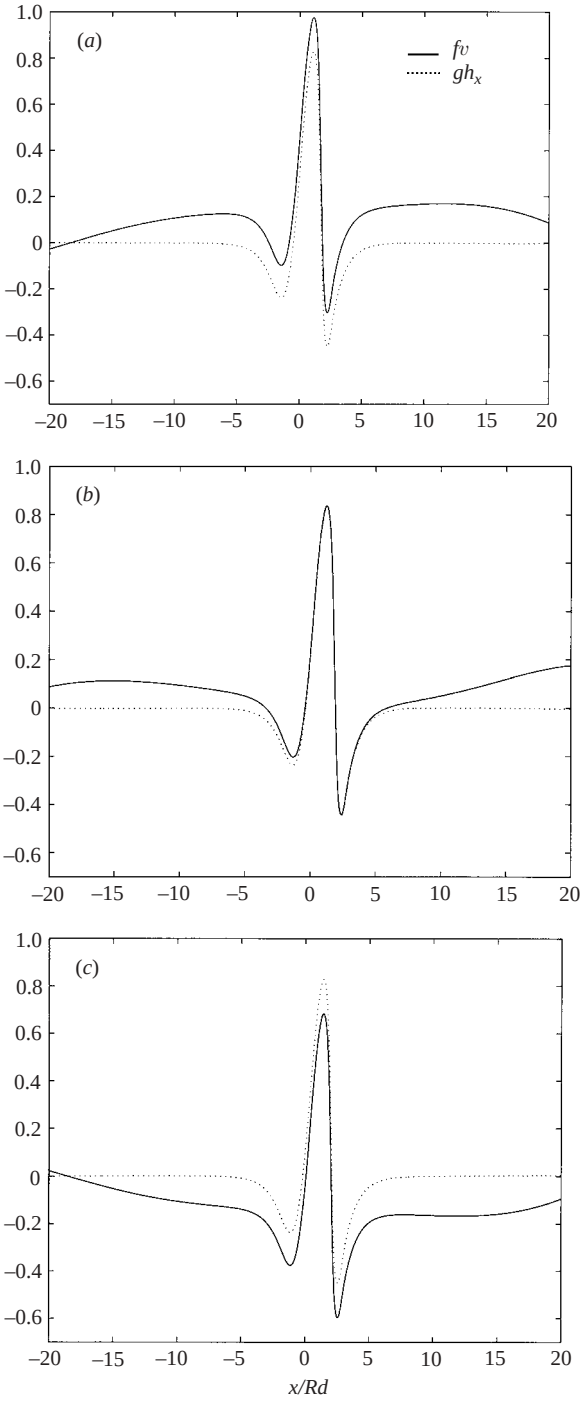


FIGURE 4. Check of balance between $fv$ and $gh_x$ in the Rossby adjustment, experiment $a$: although a state close to the geostrophic balance mean state ($b$) is rapidly achieved, oscillations persist in the jet core. The amplitude of oscillations is decreasing with time and depends on the parameters $Ro^a$ and $Bu^a$. The period of oscillations is close to $T_f$. The scale of the graphs is $c_0^2/L$. ($a$) $t/T_f = 22.0$; ($b$) 22.2; ($c$) 22.5.

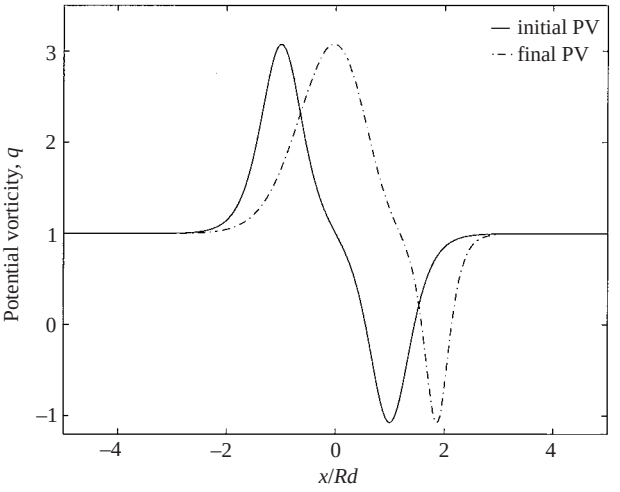


FIGURE 5. PV-shift during the Rossby adjustment process, experiment *a*. The initial distribution of PV and the mean distribution at $t = 34.2T_f$ are shown. $Ro = 1$; $Bu = 0.25$.

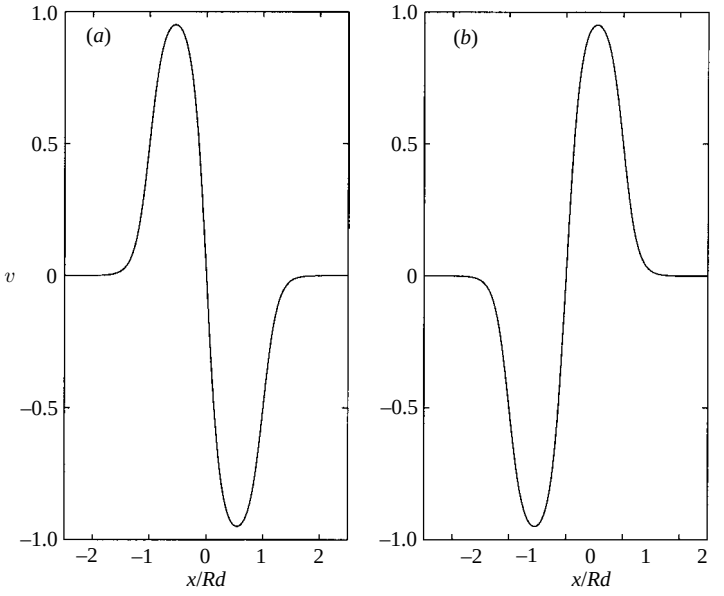


FIGURE 6. Two possible configurations of the double-jet adjustment – experiment *b*. Initial $v(x, 0)$ with (*a*) $\alpha = -1$, (*b*) $\alpha = 1$.

are:

$$-U[hu] + [hu^2 + gh^2/2] = 0, \tag{4.1a}$$

$$-U[hv] + [huv] = 0, \tag{4.1b}$$

$$-U[h] + [hu] = 0, \tag{4.1c}$$

where $U$ is the speed of the discontinuity and $[A]$ is the jump, following a fluid particle, of any quantity $A$ across the discontinuity. These conditions do not depend on the

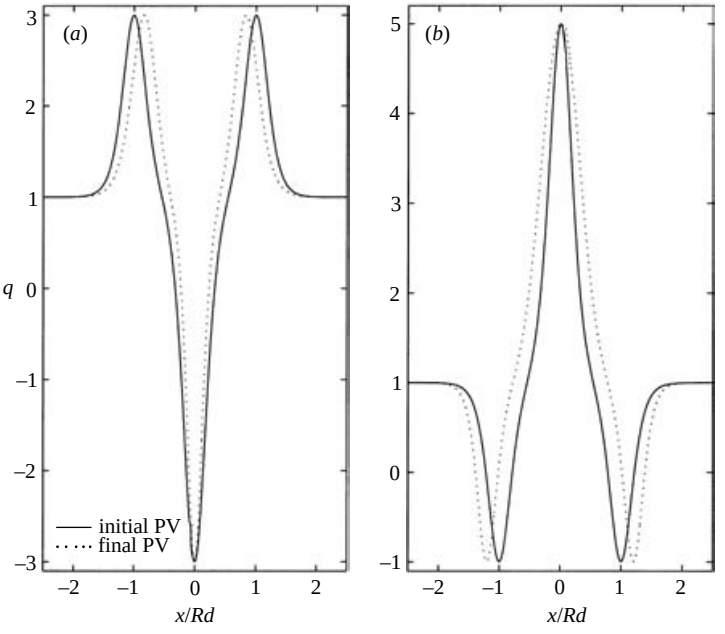


FIGURE 7. PV-shift in the double-jet adjustment: experiment $b$ with $Bu^b = 1$ and $Ro^b = 1$. PV advection, $(a)$ $\alpha = -1$, $(b)$ $\alpha = 1$.

Coriolis parameter $f$ and express, respectively, the conservation of momentum in the $x$- and $y$-directions and mass conservation across the discontinuity. Yet, physically relevant solutions are not specified unless the dissipation of the total energy $E$ across the discontinuity is ensured (cf. Whitham 1974):

$$-U[E] + [(E + gh^2/2)u] \leqslant 0 \quad \text{with} \quad E = \tfrac{1}{2}h(gh + u^2 + v^2), \tag{4.2}$$

which is an analogue of the gas dynamics entropy condition. As a direct consequence, this implies that $[h] > 0$ across a shock. Note that conditions (4.1) are satisfied by any finite-volume numerical scheme, whereas the fulfilment of condition (4.2), which is not straightforward, requires special care. From the RH and entropy conditions, it follows that the rate of the energy dissipation in every material volume $V(t)$ which contains a discontinuity depends on the amplitude of the jump only

$$\frac{\mathrm{d}}{\mathrm{d}t}\int_{V(t)} E\,\mathrm{d}x = \tfrac{1}{4}g\,[h]^2\,[u]\,. \tag{4.3}$$

We present in figure 8 the shock-induced energy decay in the Rossby adjustment experiment $a$. Note that up to 10% of the available energy is dissipated by the shock under certain circumstances. In spite of this figures 5 and 7 suggest that the PV field is not affected by dissipation due to the passage of shocks. Kuo & Polvani (1997) observed this feature in their simulations and inferred that it was due to the decrease in the shock strength induced by rotation.

Following Pratt (1983, 1984) and Peregrine (1998), in the absence of contact discontinuities, i.e. for $[v] = 0$, we consider the jump in PV equation $-U[hq] + [huq] = 0$ and continuity equation $[(U-u)h] = 0$ to obtain $(U-u)h[q] = 0$. Hence $[q] = 0$ in one dimension. Only transverse variation in shock strength can affect the PV in this framework (cf. Pratt 1983). Hence, in the $y$-independent reduction of the shallow-water equations, no PV deposit by shocks is possible.

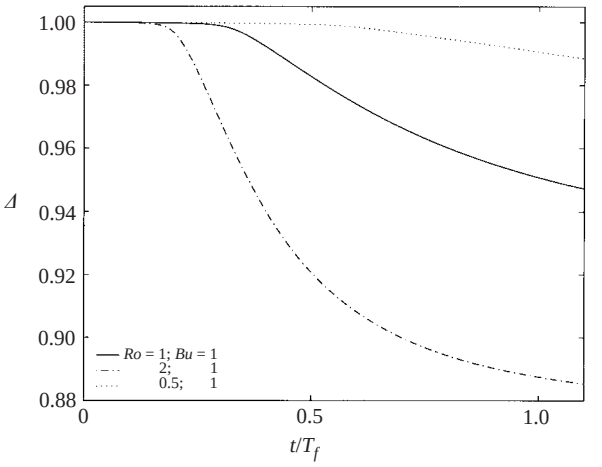


FIGURE 8. Shock-induced energy decay in the Rossby adjustment simulations: experiment *a*. The evolution of the non-dimensional energy anomaly $\Delta = (e - e_p(0))/e_p(0)$ with $e_p(t) = \int \mathrm{d}x\, g(h-H)^2/2$ and $e(t) = e_p(t) + \int \mathrm{d}x\, h(u^2+v^2)/2$ computed in the volume $[-5L, 5L]$. Note the good numerical conservation of energy at early stages (giving a criterion for detecting the shock formation). As $Ro^a$ increases, shocks appear earlier and the amount of dissipated energy increases.

As shown by Houghton (1969), shocks are modified by rotation. This implies a decrease in shock strength with time, but, as shown above, shocks do not affect the vortical part of the flow.

We can now investigate which conditions favour the shock formation on the basis of the semi-quantitative criteria for wave-breaking found in Part 1.

### 4.2. *Cyclone/anticyclone asymmetry in the adjustment of the wave perturbation of a single jet*

The first numerical experiment (experiment *c*, cf. Appendix B) along these lines is that of adjustment of a PV-less wave perturbation superimposed onto a simple balanced jet. The aim of experiment *c* is to check how the vorticity in the jet region influences shock formation. The details of the initialization are given in Appendix B. The parameters are the Rossby and the Burgers numbers associated with the jet, $Ro^c_{jet}$, $Bu^c_{jet}$ and the Rossby and the Froude numbers which specify the perturbation, $Ro^c_p$, $Fr^c_p$, cf. Appendix B. The typical evolution of the perturbation is shown in figure 9. The perturbation splits into a left and a right propagating part, but, in this case, only the former breaks inside the jet. Let us recall that, as shown in Part 1, two factors lead to breaking: strong enough gradients of the Riemann invariants and strong enough anticyclonic shear. The perturbation is small enough in figure 9, and the derivatives $R_\pm$ of the Riemann invariants rewritten in Eulerian variables (these expressions are obtained by a change of variables from corresponding expressions in Lagrangian coordinates calculated in Part 1),

$$R_\pm = 8\left(\frac{H}{h}\right)^{1/4} u_x \pm \sqrt{\frac{g}{H}}\left(\frac{h}{H}\right)^{3/4} h_x, \tag{4.4}$$

are dominated by the derivative ofthe height field (the second term). Since the sign

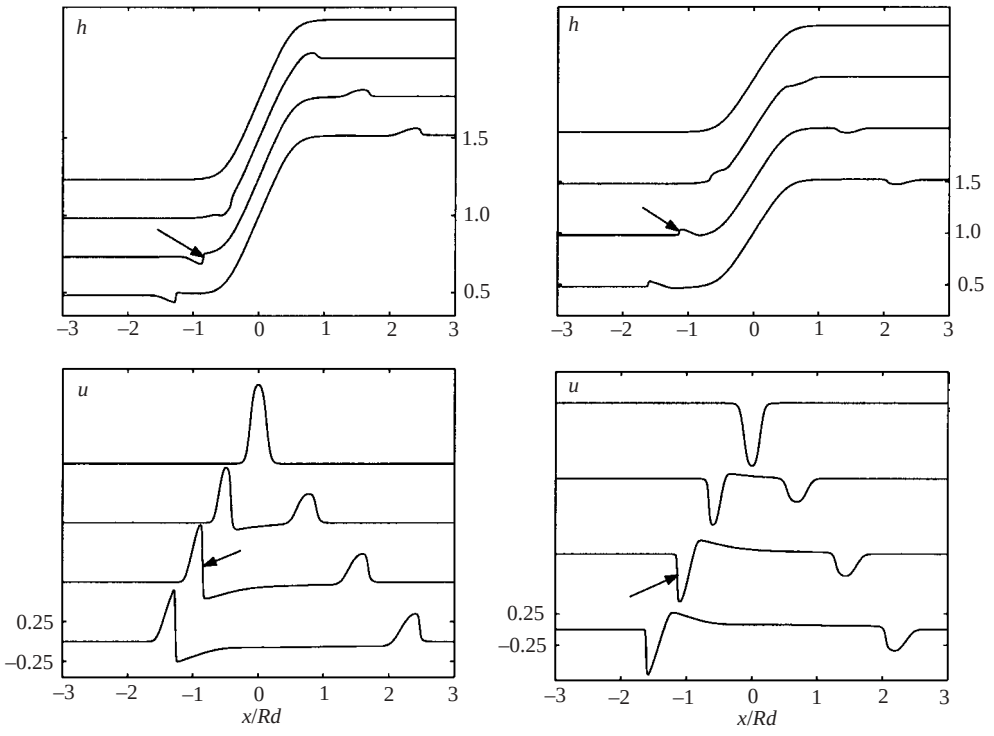


FIGURE 9. Wave breaking in a simple jet: experiment $c$ with $Ro^c_{jet}=1$, $Bu^c_{jet}=1$ and $Ro^c_p=0.8$. Left-hand column: $h, u$ in the case $u_p > 0$. Right-hand column: $h, u$ in the case $u_p < 0$. In both cases, the fields are plotted for successive times $0, 0.1, 0.2, 0.3\,T_f$ ( from top to bottom ). The arrows indicate shock locations. The vertical scale is given for the lowermost curves, it is the same for other curves.

of this term is fixed by the geostrophic balance of the basic state, the part of the perturbation propagating toward the small $h$ region is more likely to break. Hence, breaking happens at the cyclonic part of the balanced jet as the influence of anticyclonicity is overcome by the strength of pressure gradients in this case.

### 4.3. *The influence of background vorticity*

In order to find how the region of negative relative vorticity could force the wave-breaking we carry out the experiment $d$, cf. Appendix B. The initial conditions correspond to a balanced double-jet with a superimposed wave perturbation. We fix the following parameters: $Ro^d_{jet}$, $Bu^d_{jet}$, $Ro^d_p$, $Fr^d_p$ and let $\alpha^d$ take three different values so that we can test the influence of vorticity on the wave-breaking. The three cases are represented in figure 10. In each case, the wave-perturbation scale is chosen so that the perturbation is located in the constant $h$ region, $h = H$. More precisely, in all cases, the quantity $R_\pm$ is the same initially. Finally, the perturbation is small enough to consider that the Eulerian and Lagrangian coordinates coincide. The evolution of the wave-field in the test case $\alpha^d = 0$ where the background flow is constant is shown in figure 11. The perturbation splits into two, propagating in the opposite sense parts. Each evolves independently and breaks before $t = T_f/2$. Note that we need not consider the symmetric case with positive initial $u_p$ because the system (2.6) is invariant under the change of variables $u \to -u$, $x \to -x$. Now let us consider two other cases: for $\alpha^d > 0$ ($\alpha^d < 0$), the perturbation propagates first through a region of positive

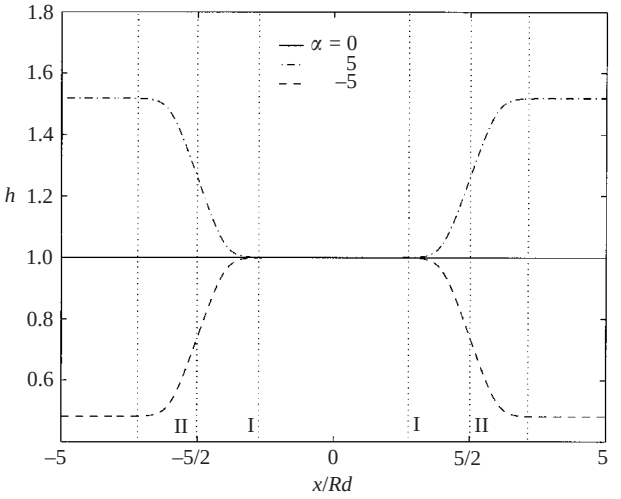


FIGURE 10. Background state for three cases of the adjustment of wave-perturbations over a balanced double-jet: experiment $d$, with $Ro^d_{jet} = 0.5$, $Bu^d_{jet} = 1$. The height at the centre is the same and equal to $H$ in the three cases. If $\alpha^d > 0$ ($< 0$), the regions labelled $I$ and $II$ correspond to positive (negative) and negative (positive) relative vorticity regions, respectively.

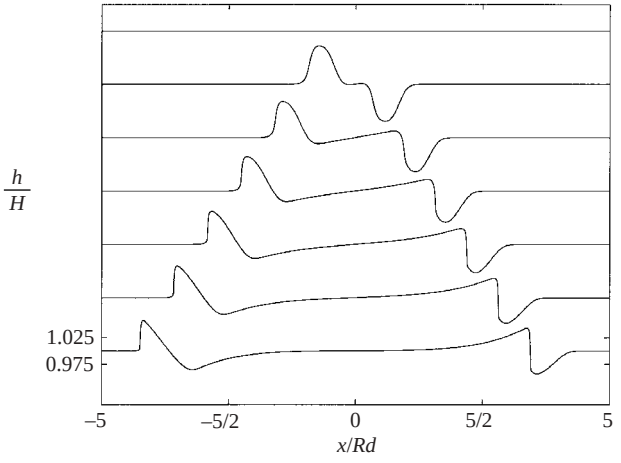


FIGURE 11. Time evolution of the height field in the wave adjustment: experiment $d$ with $\alpha^d = 0$, $Ro^d_p = -0.15$, $Fr^d_p = -0.15$ and no background jet. $h$ is plotted for successive times: 0, 0.1, 0.2, 0.3, 0.4, 0.5, 0.6 $T_f$ (from top to bottom). The arrows indicate shock locations. The vertical scale is given for the lowermost curves, it is the same for other curves.

(negative) vorticity. The analysis of Part 1 suggests that breaking would be favoured in the second case $\alpha^d < 0$, and this is indeed what happens: figure 12 is a snapshot of the field at $t = 0.35T_f$ when the perturbation has propagated through the region $I$. As we can see, the gradients become steeper as $\alpha^d$ decreases. This is observed for the field $u$, but also for the field $hu$, so this effect is not due to the mass variation. Although this simulation indicates that the negative vorticity region favours breaking, there is no clear-cut separation between the effect of vorticity and that of large gradients, because the geostrophic balance implies a relation between $h_{xx}$ and $v_x$. Therefore, $R_{\pm}$

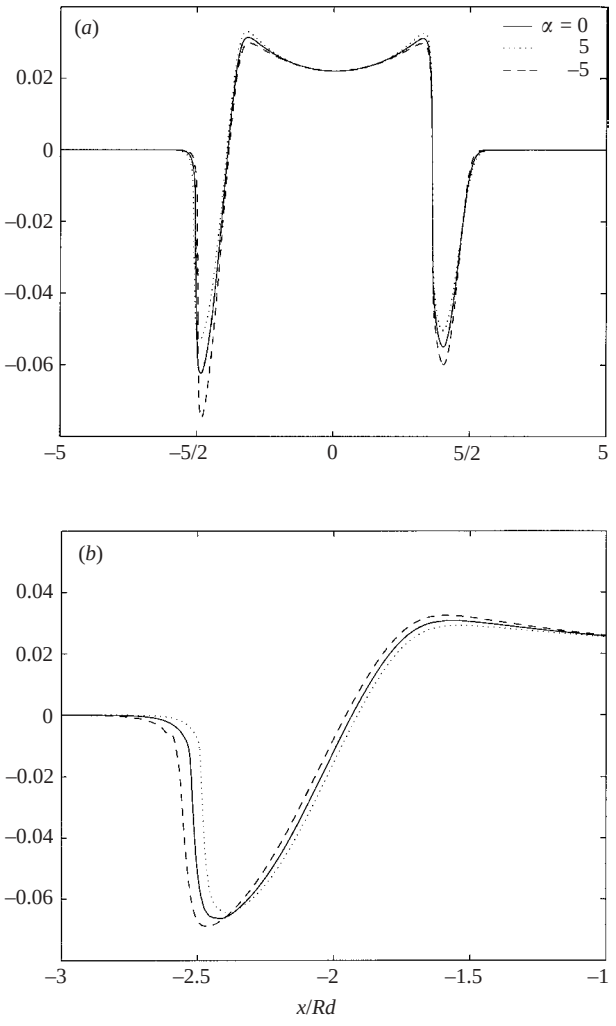


FIGURE 12. Influence of the background vorticity on the wave breaking – experiment $d$ with $Ro^d_{jet} = 0.5$, $Ro^d_p = -0.15$, $Fr^d_p = -0.15$: ($a$) $u$ is plotted at time $t = 0.35T_f$ for the three cases: $\alpha^d = 0$, $\alpha^d = 5$, $\alpha^d = -5$. At $t = 0.35T_f$, the perturbation has passed through a region of vorticity whose sign depends on the sign of $\alpha^d$. The gradients are becoming steeper as $\alpha^d$ decreases. ($b$) The same result holds for $hu$. It is found that if $\Lambda$ is the maximum amplitude of $hu$ for $\alpha = 0$, then for $\alpha^d = 5$ the amplitude is $1.04\Lambda$ and for $\alpha^d = -5$ it is $0.96\Lambda$.

varies due to $v_x$, but also because of the variation $h_x$. Note that the main effect is a delay induced by the variation of $h$: the wavefront is becoming more rapid as $h$ diminishes, which explains the shift between the plots in figure 12 . The final remark is that $[h]$ decreases as the perturbation is going through a region of negative vorticity and increases in positive vorticity regions. This suggests that although breaking itself is only slightly influenced by cyclonicity, the dissipation is substantially enhanced in such regions.

### 4.4. *Summary of the shock-formation simulations*

(i) Shock formation events are ubiquitous;
(ii) shocks induce energy loss which can affect up to 10% of the available energy;

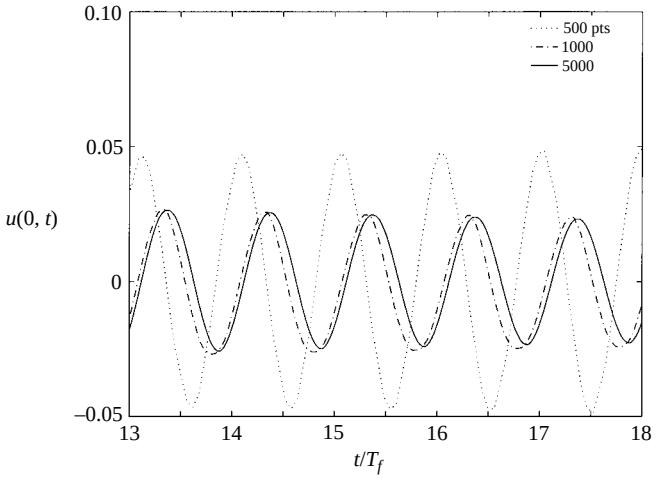


FIGURE 13. Grid refinement impact on long-time computation: experiment $d$ with $Ro^d = 0.25$, $Bu^d = 1$, $Ro_p^d = -0.5$ and $Fr_p^d = -0.5$. Both amplitude and frequency obtained vary until sufficient numerical resolution is achieved (solid line). The number of grid-points is being increased within the fixed spatial domain $[-40R_d, +40R_d]$ giving the corresponding spatial resolutions $\Delta x = 0.16R_d, 0.08R_d, 0.016R_d$, respectively.

(iii) PV is not modified by the dissipation due to shocks;
(iv) in a simple balanced jet, breaking is more likely to occur at the *cyclonic* side.

## 5. Adjustment and quasi-inertial oscillations

One of the most important questions about the geostrophic adjustment is whether it is complete. It was shown in Part 1 that no trapped modes are possible within the localized jets/fronts in the model (2.1), but that for certain configurations the non-monotonicity of the 'potential' in the effective Schrödinger-like equation governing the dynamics of small perturbations over a balanced state may delay the dispersion of the initial perturbation (so-called quasi-stationary states (QSS) may exist). Both results were based on the smallness of the wave-perturbations over the balanced jet/front, so the question of completeness of adjustment in the case of a fully nonlinear perturbation was not definitely answered. The quasi-inertial oscillations were observed in experiments *a* and *b*, and earlier in the simulations of Kuo & Polvani (1997). In order to understand the nature of these oscillations, we performed long-time simulations and undertook special efforts to determine the form of the relaxation law. Let us recall that the standard dispersion means a $t^{-1/2}$ law and that we could expect (cf. Part 1) exponential corrections due to quasi-stationary states, if any. The non-decay of the oscillations amplitude would mean wave-trapping.

In order to keep the number of parameters reasonable, we consider here an initial imbalance with the same characteristic scale $L$ as the jet itself and use the same perturbation as in experiment *d*.

### 5.1. *Technical limitations on long-time computation*

Before proceeding, it is worth making a brief comment on numerics. It is clear that long-time numerical simulations must be done with great care because of the accumulation of numerical errors. In order to illustrate the effect of spatial resolution on the long-time behaviour of the solution, we plotted in figure 13 the field $u$ at point

$x = 0$ versus time for the same experiment with increasing spatial resolution. For example, from a rough-resolution simulation, we might deduce that the decay law is exponential, whereas with a finer grid the law $t^{-1/2}$ is obtained. (Increasing resolution further beyond the highest one displayed does not change either amplitude or phase of the oscillations – see Appendix B for numerical convergence tests.) Hence, any result on the amplitude of the oscillations has to be checked on a refined computation grid, which we have been doing systematically. Another way to improve the behaviour of the scheme for long-time computations is to use an $o(\Delta t)^2$ time-stepping scheme instead of the $o(\Delta t)$ classical Euler scheme. In our simulations, this was done for Method 2 (cf. Appendix A.4).

### 5.2. *Dispersion of the wave packets superimposed on the jet*

As was shown in Part 1, the spatial structure of small-amplitude disturbances over a balanced state is governed by the Shrödinger-like equation:

$$\frac{\mathrm{d}^2\psi}{\mathrm{d}a^2} + k_\psi^2(a)\psi = 0, \tag{5.1}$$

where $a$ is the mass Lagrangian variable, and $\psi$ is the amplitude of the wave field. The possibility of having a modified dispersion of a (small) perturbation depends on the presence of a potential well (and, hence, of related QSS) in pseudo-potential $k_\psi^2$. We rewrite the pseudo-potential in Eulerian variables as:

$$k_\psi^2 = \frac{H^3}{h^3}\left(\frac{\omega^2 - f^2}{gH} - \frac{3}{2}\frac{\partial^2}{\partial x^2}\frac{h}{H} + \frac{3}{4}\frac{H}{h}\left(\frac{\partial}{\partial x}\frac{h}{H}\right)^2\right). \tag{5.2}$$

In what follows, the same initial wave-perturbation is used in three different cases and superimposed onto different background-adjusted states corresponding to the following situations labelled with the help of parameter $\alpha$ in the framework of experiment $d$:

(i) $\alpha = 0$, a uniform PV state;
(ii) $\alpha = 1$, a negative mass anomaly;
(iii) $\alpha = -1$, a positive mass anomaly.

The pseudo-potential $k_\psi^2$ is plotted for the last two cases in figure 14. If $\alpha = 0$, it is uniform: $k_\psi^2 = (\omega^2 - f^2)/c^2$ and no QSS is possible. If $\alpha \neq 0$, QSS are expected at frequency $\omega$ if the potential $k_\psi^2$ is positive in a localized region and negative elsewhere. The relaxation laws of the same initial perturbation as in experiment $d$ are presented in figure 15. They are obtained as follows. For each case $\alpha = 0, 1, -1$ we sampled the momentum density $hu(0, t)$ with 5000 points. We then computed $A(\omega, t)$, the windowed discrete-time Fourier transform of this signal, using a sliding Hann window of 256 points with an overlapping of 128 points, and plotted $A(f, t)$.

All three curves exhibit a dispersive $\propto \lambda/\sqrt{t}$ decay with $\lambda$ depending on the vortical part of the flow. Therefore, the tentative correction to the standard dispersion law due to QSS is negligible for the initial configuration of a flow with comparable characteristic scales of balanced and imbalanced parts which we use. Hence, the nature of quasi-inertial oscillations detected in previous simulations becomes clear: they are simply the extra-long IGW having almost zero group velocity and, thus, are almost non-propagative.

### 5.3. *Summary of the results on decay of quasi-inertial oscillations*

(i) In all cases studied, the relaxation of the initial wave-packet follows the $t^{-1/2}$ law and is not sensitive to the complex structure of the underlying vortex flow;

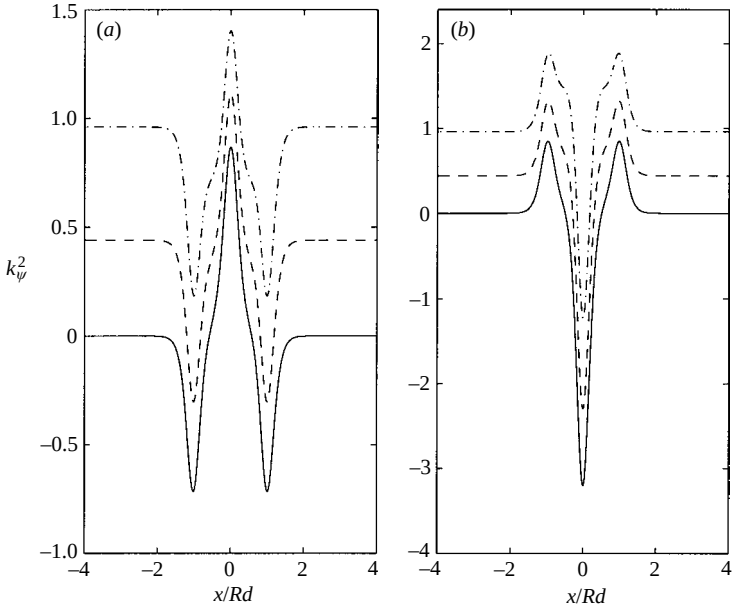


FIGURE 14. Potential $k_\psi^2$ – experiment $d$ with $Ro^d = 0.25$ and $Bu^d = 1$. For each case $k_\psi^2(\omega)$ is plotted for $\omega = f$ (solid), $\omega = 1.2f$ (dashed) and $\omega = 1.4f$ (dash-dotted). QSS are expected at frequency $\omega$ if $k_\psi^2(\omega) > 0$ in a bounded domain surrounded by a region where $k_\psi^2(\omega) < 0$, i.e. in the case $\omega = f$, $\alpha = -1$, which corresponds to a positive mass anomaly. ($a$) $\alpha = -1$, ($b$) $\alpha = 1$.

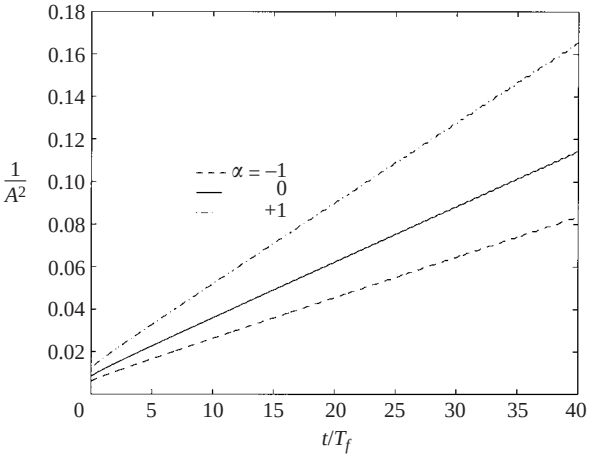


FIGURE 15. Relaxation laws for a double-jet configuration in three cases – experiment $d$ with $Ro^d = 0.25$, $Bu^d = 1$, $Ro_p^d = -0.5$ and $Fr_p^d = -0.5$. The plotted quantity is $1/A^2$, where $A$ is the time-dependent amplitude of the Fourier harmonics with $\omega = f$. In all cases, the relaxation law is $\lambda/\sqrt{t}$ with $\lambda = 19.43$ for uniform rest flow ($\alpha = 0$); $\lambda = 16.15$ for negative mass anomaly ($\alpha = 1$); $\lambda = 22.74$ for positive mass anomaly ($\alpha = -1$).

(ii) the characteristic time-scale of decay is determined by the vortex part of the flow.

## 6. Adjustment and exact nonlinear wave solutions in the periodic domain

In this section, we study the geostrophic adjustment in the periodic domain, and focus on the interaction between shocks and exact periodic nonlinear wave solutions

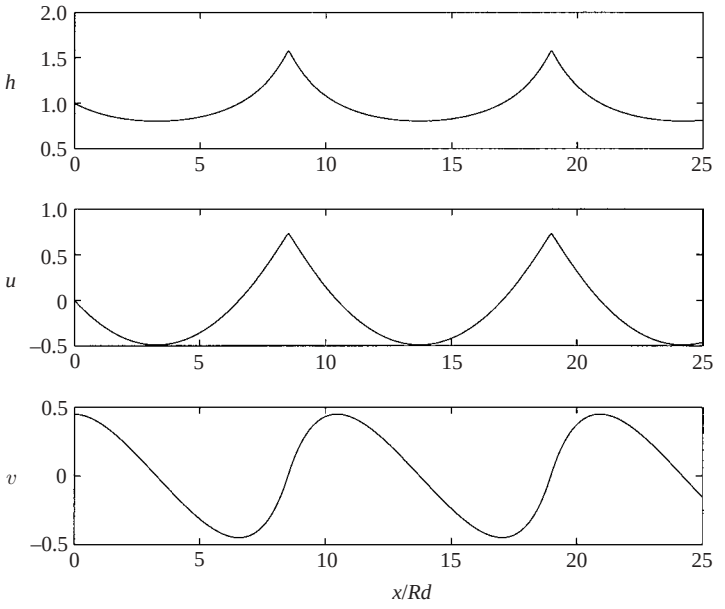


FIGURE 16. Exact nonlinear-wave solution used in experiment $e$; the limiting-amplitude configuration with the phase-speed $c = 2c_0$ (cf. Part 1) is chosen.

known to exist in 1dRSW. These solutions, found by Shrira 1981, 1986 (the idea appeared first in Ostrovsky 1978) and described later from the Lagrangian viewpoint in Part 1, are steady propagating finite-amplitude periodic waves. It is worth recalling that their amplitudes are limited from above by some limiting profile, whereas in the limit of vanishing amplitudes the ordinary linear IGW are recovered (cf. Part 1). Although these solutions were discovered a long time ago, little is known on their stability. The interaction of these nonlinear waves with shocks is another open question. Recall that, at finite amplitudes, these waves are 'supersonic' (cf. Part 1). So we start our study by investigating stability of the nonlinear periodic wave solutions. We limit ourselves in this section by constant-PV, i.e. purely wave (although fully nonlinear) configurations, as is the case for the exact nonlinear periodic waves themselves.

### 6.1. *Stability of the nonlinear periodic waves*

In figure 16, we plotted an exact nonlinear wave solution of limiting amplitude with the phase speed $c = 2c_0$ in physical space. This solution is used to initialize the Cauchy problem with a perturbation superimposed on it (experiment $e$). The fact that our numerical scheme maintains this solution for a long time in the absence of the perturbation was one of the principal tests of the code. We then look at what time we can observe a significant discrepancy between the exact and perturbed solutions. This experiment, of course, is not an exhaustive study of stability, but rather a first check of the robustness of the solution.

The evolution of the height field of the nonlinear wave with a localized perturbation applied at the initial moment is presented in figure 17 and shows that nonlinear waves are indeed robust.

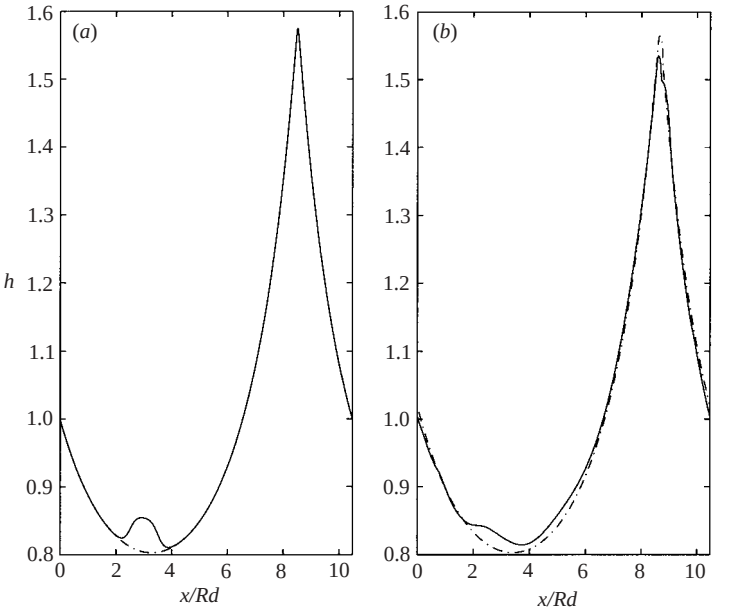


FIGURE 17. Stability of the nonlinear wave solution of limiting amplitude, experiment $e$: ($a$) localized perturbation is added to the nonlinear wave solution; ($b$) the resulting profile after ten inertial periods. Between these two snapshots, the wave propagates at speed $c = 2c_0$ so that 12 recurrences in the computation domain were observed.

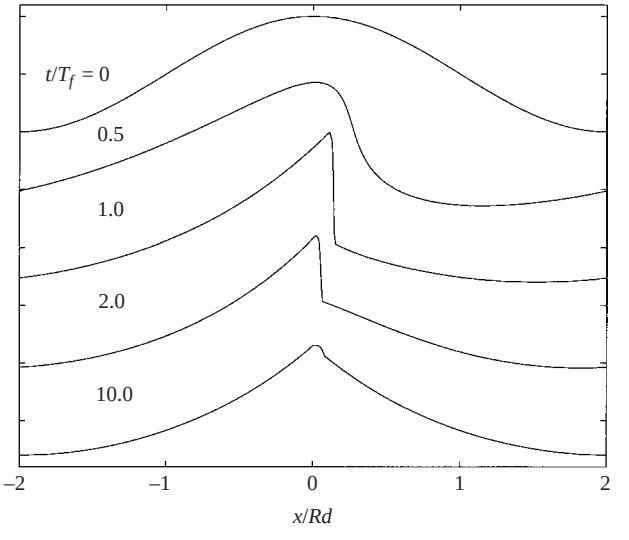


FIGURE 18. Time evolution of a finite-amplitude harmonic wave, experiment $f$. $Ro = 0.1, k = \pi/2$.

### 6.2. *Evolution of a finite-amplitude harmonic wave and emergence of nonlinear periodic waves*

In figure 18, we show that nonlinear periodic waves emerge spontaneously during the evolution of a finite-amplitude harmonic wave.An exact harmonic solution to the

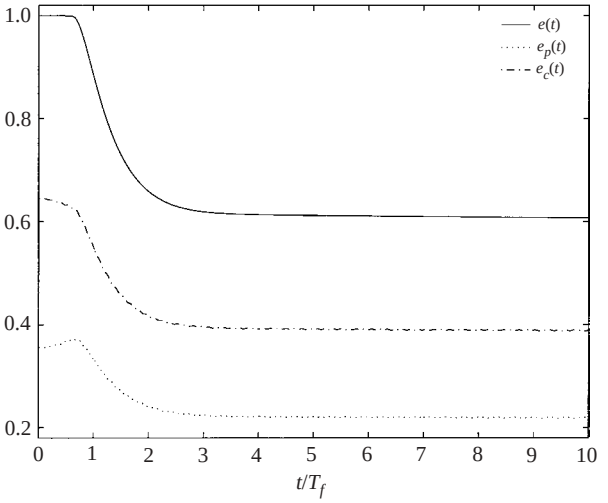


FIGURE 19. Energy decay during the evolution of a high-amplitude harmonic wave, experiment $f$. We show the evolution of the non-dimensional total energy $e/e(0)$, of the non-dimensional available kinetic energy $e_p/e(0)$ and of the non-dimensional kinetic energy $e_c/e(0)$, with $e_p(t) = \int \mathrm{d}x\, g(h-H)^2/2$, $e_c(t) = \int \mathrm{d}x\, h(u^2+v^2)/2$ and $e = e_p + e_c$ computed in the whole periodic domain. $Ro = 0.1$, $k = \pi/2$.

linearized equations (2.1) with $Ro^e = 0.1$ and $k = \pi/2$ is taken as the initial condition in experiment $f$. As seen from figure 18, the initial wave breaks down and, after a stage of geostrophic adjustment, a quasi-steady propagative state is reached which resembles closely the cusp pattern of the exact propagative nonlinear solution. The adjustment is achieved through shock formation and related energy dissipation. The energy decay due to dissipative processes in the shock is displayed in figure 19 and shows that in this case the energy tends to a nearly steady value after a rapid stage of adjustment.

### 6.3. *Summary of the periodic domain study*

We thus find indications that nonlinear periodic waves of limiting amplitude are nonlinearly stable. They arise naturally during nonlinear adjustment in the periodic domain and are, probably, attractors. The proof of this hypothesis requires further work.

## 7. Summary and discussion

Thus, from our high-resolution shock-capturing numerical simulations we derive the following general properties of the fully nonlinear geostrophic adjustment in 1dRSW:

(i) For localized initial data in the open domain, the adjusted state is reached even for non-positive-definite initial PV distributions;

(ii) The geostrophic adjustment is always complete; it is a rapid process: the final distribution of PV is achieved within several inertial periods. However, owing to their feeble group velocity the quasi-inertial oscillations, although being dispersed according to the standard dispersion law $\sim 1/\sqrt{t}$, stay in the vicinity of the initial perturbation for a long time;

(iii) Shock formation within or in the immediate vicinity of the jet core is ubiquitous. Together with outgoing IGW, shocks provide an effective means (the only one in the

| | Method 1 | Method 2 |
|---|---|---|
| Solver | Roe approximate Riemann solver | Relaxation scheme |
| Source terms | Quasi-steady wave-propagation method | Non-split method |
| Conservative | Yes | Yes |
| Positiveness of $h$ | Not guaranteed | Guaranteed |
| Steady solutions | Preserved | Preserved |
| $O(\Delta x)^n$ | $n = 2$ | $n = 2$ |
| $O(\Delta t)^n$ | $n = 1$ | $n = 2$ |

TABLE 1. Numerical schemes and their basic properties.

periodic geometry) for the flow to evacuate the excess energy and to arrive to an energy-minimum balanced state;

(iv) Adjustment in the periodic domain gives rise to spontaneous emergence of exact nonlinear periodic waves of limiting amplitude after the excess energy is dissipated via shocks. Nonlinear wave solutions are found to be robust.

The scenario of geostrophic adjustment obtained above is, obviously, subject to the limitations due to the choice of the model. However, we focused on nonlinearity-dominated adjustment and RSW is a good conceptual model for this purpose. Of course, the physical wave-breaking processes are not resolved in the model, but parameterized by the shock (hydraulic jump) formation. Needless to say, shocks are formally beyond the limits of applicability of the hydrostatic shallow-water approximation which is derived under the hypothesis of horizontal scales of motion being much larger than the fluid depth. Nevertheless, the parameterization of localized dissipation regions produced by wave-breaking in terms of shocks is widely used (cf. e.g. Whitham 1974). It is mathematically consistent and allows high-resolution numerical simulations, as illustrated above. Going beyond the hydrostatic shallow-water approximation (which would add physical realism, but reduce mathematical tractability) is out of the scope of the present paper. Let us only mention that work is in progress on the nonlinear adjustment in two- and three-layer RSW and will be reported elsewhere.

The work of J. L. S. and V. Z. was supported by the French National Program PATOM and ACI PCN. We are grateful to anonymous referees for their constructive remarks on the original version of the paper.

## Appendix A. Numerical methods

We used two different finite-volume methods to investigate the time-evolution of initial imbalanced states in 1dRSW. We briefly present below the basic procedures. Higher-order corrections are computed in both cases so that second-order spatial accuracy is obtained for each method. However, we will not describe these corrections explicitly in this Appendix. Euler time-stepping is used for both cases, except for long-time computations where second-order time accuracy is needed. A summary of the main features and properties of each method is given in table 1.

### A.1. *Method* 1

*The wave-propagation method*

The basic numerical procedure which is used to capture discontinuous solution to one-dimensional systems of conservation laws is the Godunov method as

implemented in the CLAWPACK package. Details are given in LeVeque (1992) or in the CLAWPACK documentation, 2002 (Version 4.1, available at http://www.amath.washington.edu/claw/). A conservative system,

$$U_t + f(U)_x = 0, \tag{A 1}$$

with $U \in R^n$, is discretized, following a finite-volume method, on a uniform grid with $\Delta x = x_{j+1} - x_j$. We consider piecewise-constant states in each mesh cell, with discontinuities at each interface. This defines a series of local Riemann problems consisting of the breakup of a single interface discontinuity. The following first-order conservative numerical scheme in the $j$th cell for $t_n = n\Delta t$ results:

$$U_j^{n+1} = U_j^n - \frac{\Delta t}{\Delta x}\left(F\left(U_j^n, U_{j+1}^n\right) - F\left(U_{j-1}^n, U_j^n\right)\right), \tag{A 2}$$

where $F$ is the numerical flux function which is evaluated from the exact or approximate solution of the Riemann problem. This solution is composed of three waves (two sonic disturbances and a contact surface) separating three states. The integration of these waves over a mesh cell gives the numerical flux. The part of the code designed to calculate the numerical flux is the Riemann solver. Note that since we apply the Godunov method to the conservative system (2.6), the numerical integration will give an approximate solution of the Cauchy problem which conserves mass and momentum.

Within the CLAWPACK implementation, the Godunov method is written in a form that requires no explicit computation of the waves. Instead, it uses a flux difference splitting (see LeVeque 1997 for details), which is a decomposition of $f(U_{j+1}) - f(U_j)$ into a left-going flux difference (say $\Delta^-_{j+1/2}$) and a right-going flux difference (say $\Delta^+_{j+1/2}$) with the property that:

$$\Delta^-_{j+1/2} + \Delta^+_{j+1/2} = f(U_{j+1}) - f(U_j), \tag{A 3}$$

so the scheme is finally written:

$$U_j^{n+1} = U_j^n - \frac{\Delta t}{\Delta x}\left(\Delta^+_{j-1/2} + \Delta^-_{j+1/2}\right). \tag{A 4}$$

We can obtain higher-order schemes by applying flux-limiting correction (cf. LeVeque 1992); the present study is carried out with a second-order accuracy. The 1dRSW is solved with the Roe solver; this linearized Riemann solver calculates an approximate solution to the exact nonlinear Riemann problem that consists of pure discontinuities. Since the linear local equations cannot capture the rarefaction waves, an 'entropy fix' is to be applied, consisting in the addition of a small amount of dissipation which prevents formation of shocks violating the entropy condition. This typically happens when the true Riemann solution contains a transonic rarefaction wave.

*Source-terms description*

We present here the numerical procedure we used to handle the Coriolis source terms in the 1dRSW, (2.6). This method is documented in LeVeque (1998) or in CLAWPACK. It was originally developed to compute a topographic forcing in the shallow-water equations within the framework of the Godunov method.

The 1dRSW is an inhomogeneous system of conservation laws, that can be written as

$$U_t + f(U)_x = \psi(U). \tag{A 5}$$

where $f$ is a flux function and $\psi$ the source term coming from the Coriolis force. Geostrophically adjusted states correspond to situations in which the flux gradient is balanced by the source term.

The key idea of the quasi-steady wave-propagation method is to introduce a Riemann problem at the centre of each grid cell whose flux difference exactly cancels the Coriolis source term. This leads to modified Riemann problems at cell edges in which the jump now corresponds to deviations from the steady state. At $t = n\Delta t$, the jump in the $j$th cell has a magnitude $|U_j^+ - U_j^-|$ where the quantities $U_j^+$ and $U_j^-$ are defined in the left and the right half of that cell, respectively. The jump should satisfy the following conditions:

$$\left.\begin{aligned} &\tfrac{1}{2}(U_j^- + U_j^+) = U_j, \\ &f(U_j^+) - f(U_j^-) = \Delta x\, \psi(U_j). \end{aligned}\right\} \tag{A 6}$$

Then, if the time step $\Delta t$ is small enough, the scheme will preserve steady states (LeVeque 1998). The first condition ensures that the method remains conservative by leaving the cell average unchanged; the second says that the waves emanating from the cell-centred Riemann problem exactly cancel the influence of the source. As noticed by LeVeque (1998), this treatment of the source fails if the solution contains a transonic shock, namely with propagation velocity changing sign during evolution.

### A.2. *Method* 2

This method for solving (2.6) has two ingredients: a method for solving the shallow-water system with topography, and a procedure to interpret the rotation term as an apparent topography.

*Well-balanced schemes for shallow-water with topography*

Before considering the 1dRSW system, let us introduce the shallow-water system with topography that was much studied in relation with numerical schemes:

$$\left.\begin{aligned} &h_t + (hu)_x = 0, \\ &(hu)_t + (hu^2 + gh^2/2)_x + hZ_x = 0. \end{aligned}\right\} \tag{A 7}$$

Here, $Z(x)/g$ represents topography. In this system, the steady states given by $u = 0$, $gh + Z = const$, play a crucial role. In the past few years, a large amount of work has been done on the problem of finding well-balanced schemes for (A 7), which means that they need to preserve steady states at the discrete level. According to Bouchut (2004), such schemes can be written as

$$U_i^{n+1} - U_i^n + \frac{\Delta t}{\Delta x}\left(F_{i+1/2-} - F_{i-1/2+}\right) = 0, \tag{A 8}$$

where $U_i^n$ is an approximation of $U = (h, hu)$, and the left/right numerical fluxes are computed as

$$F_{i+1/2-} = F_l\left(U_i, U_{i+1}, \Delta Z_{i+1/2}\right), \qquad F_{i+1/2+} = F_r\left(U_i, U_{i+1}, \Delta Z_{i+1/2}\right), \tag{A 9}$$

with $\Delta Z_{i+1/2} = Z_{i+1} - Z_i$. The numerical fluxes $F_l$ and $F_r$ must satisfy two consistency properties. The first is the consistency with the conservative term,

$$F_l(U, U, 0) = F_r(U, U, 0) = F(U) \equiv (hu, hu^2 + gh^2/2), \tag{A 10}$$

and the second is the consistency with the source,

$$F_r(U_l, U_r, \Delta Z) - F_l(U_l, U_r, \Delta Z) = (0, -h\Delta Z) + o(\Delta Z), \tag{A 11}$$

as $U_l$, $U_r \to U$ and $\Delta Z \to 0$. An overall property that we require is the conservation of mass,

$$F_l^h(U_l, U_r, \Delta Z) = F_r^h(U_l, U_r, \Delta Z) \equiv F^h(U_l, U_r, \Delta Z). \tag{A 12}$$

The property for the scheme to be well-balanced is that

$$\left.\begin{aligned} &F_{i+1/2-} = F(U_i), \quad F_{i+1/2+} = F(U_{i+1}), \\ &\text{whenever } u_i = u_{i+1} = 0, \quad g h_{i+1} - g h_i + \Delta Z_{i+1/2} = 0. \end{aligned}\right\} \tag{A 13}$$

A consistent well-balanced scheme that is very cheap, that is able to treat transonic flows and dry states $h = 0$, and that satisfies a discrete entropy inequality, has been proposed recently by Audusse *et al.* 2003. It has the following form,

$$\left.\begin{aligned} F_l(U_l, U_r, \Delta Z) &= \mathscr{F}(U_l^*, U_r^*) + \begin{pmatrix} 0 \\ g h_l^2/2 - g h_{l*}^2/2 \end{pmatrix}, \\ F_r(U_l, U_r, \Delta Z) &= \mathscr{F}(U_l^*, U_r^*) + \begin{pmatrix} 0 \\ g h_r^2/2 - g h_{r*}^2/2 \end{pmatrix}, \end{aligned}\right\} \tag{A 14}$$

where $U_l^* = (h_{l*}, h_{l*} u_l)$, $U_r^* = (h_{r*}, h_{r*} u_r)$, and

$$h_{l*} = \max(0, h_l - \max(0, \Delta Z/g)), \qquad h_{r*} = \max(0, h_r - \max(0, -\Delta Z/g)). \tag{A 15}$$

Here, $\mathscr{F}$ is any entropy satisfying consistent numerical flux for the homogeneous problem (i.e. with $Z = const$), that is able to deal with dry states. Our choice here is a relaxation solver described in Bouchut (2004), but other choices give similar results.

*Rotation as an apparent topography*

The apparent topography method that we introduce here is general and can be used to treat generic source terms. Consider for our purpose the shallow-water system with topography and Coriolis force

$$\left.\begin{aligned} &h_t + (hu)_x = 0, \\ &(hu)_t + (hu^2 + gh^2/2)_x + hZ_x - fhv = 0, \\ &(hv)_t + (huv)_x + fhu = 0, \end{aligned}\right\} \tag{A 16}$$

where $Z = Z(x)$, $f = f(x)$. Now solutions at rest are given by $u = 0$, $fv = (gh + Z)_x$. The idea is to identify the two first equations in (A 16) as (A 7) with a new topography $Z + B$, where $B_x = -fv$. Now, $v$ depends also on time while $B$ should be time independent, so we take $B_x^n = -fv^n$ and solve (A 7) on the time interval $(t_n, t_{n+1})$ with topography $Z + B^n$.

At the discrete level, this is done as follows. We define

$$\Delta B_{i+1/2}^n = -f_{i+1/2} \Delta x \frac{v_i^n + v_{i+1}^n}{2}, \tag{A 17}$$

and update $U = (h, hu, hv)$ via

$$U_i^{n+1} - U_i^n + \frac{\Delta t}{\Delta x}\left(F_{i+1/2-} - F_{i-1/2+}\right) = 0, \tag{A 18}$$

with

$$\left.\begin{aligned} F_{i+1/2-} &= \left(F_l\left(U_i, U_{i+1}, \Delta Z_{i+1/2} + \Delta B_{i+1/2}^n\right), F_{i+1/2-}^{hv}\right), \\ F_{i+1/2+} &= \left(F_r\left(U_i, U_{i+1}, \Delta Z_{i+1/2} + \Delta B_{i+1/2}^n\right), F_{i+1/2+}^{hv}\right), \end{aligned}\right\} \tag{A 19}$$

where the numerical fluxes $F_l$, $F_r$ are those associated to the problem without rotation of the previous section. The transverse momentum fluxes have a natural discretization

associated to the equivalent conservation law $(h(v+\Omega))_t + (hu(v+\Omega))_x = 0$, with $\Omega_x = f$, which is strongly related to the potential vorticity conservation. This gives the following natural formulae

$$\left(F^{hv}_{i+1/2-}, F^{hv}_{i+1/2+}\right) = \begin{cases} \left(F^h_{i+1/2} v_i,\ F^h_{i+1/2}\left(v_i - f_{i+1/2}\Delta x\right)\right) & \text{if } F^h_{i+1/2} \geqslant 0, \\ \left(F^h_{i+1/2}\left(v_{i+1} + f_{i+1/2}\Delta x\right),\ F^h_{i+1/2} v_{i+1}\right) & \text{if } F^h_{i+1/2} \leqslant 0. \end{cases} \tag{A 20}$$

Then it is easy to see that our scheme is consistent with (A 16), and well balanced since it preserves the discrete steady states satisfying $u_i = u_{i+1} = 0$ and $gh_{i+1} - gh_i + \Delta Z_{i+1/2} = f_{i+1/2}\Delta x(v_i + v_{i+1})/2$. The scheme also conserves mass, it is able to compute dry-bed states and satisfies a discrete entropy inequality. For dry-bed tests see Audusse *et al.* (2004*b*).

### A.3. *Comparison of the methods*

In order to compare the two methods, we made identical simulations within both schemes, and present in figure 20 the PV-fields we obtained. We also show the results of calculations with the operator splitting method (Method 3) used in the previous works (see e.g. Kuo & Polvani 1997). Before comparing the three runs, we should emphasize that there is no theoretical proof of the convergence (for resolution $\Delta x \to 0$) of these schemes toward the exact PV-field since the error is proved to be bounded for $(h, hu, hv)$ only.

For low resolution, the three methods give significantly different results for a relatively short-time computation, although they all converge to the same solution if resolution is increased, see the convergence tests below. At time $t/T_f = 5$, the field computed with Method 2 exactly overlaps with the refined grid reference solution obtained with maximal resolution we used – see below. However, both Method 1 and Method 3 excessively dissipate PV in certain regions. In Method 3, it is the PV maxima which are strongly dissipated (arrows A, figure 20) whereas Method 1 modifies the structure of the PV field at the wave-breaking locations (arrows B, figure 20). It should be stressed that erosion of the PV extrema increases as time evolves in Method 3; therefore, the operator splitting method is not well-suited for long-time computations. Both Method 1 and Method 2 maintain well the adjusted states and conserve PV; Method 2, in addition, preserves the structure of the PV field at the wave-breaking location. Furthermore, the three methods were compared in a series of runs with increasing resolution. The results are summarized in tables 2, 3 and 4. In each table, $\Delta x$ is the spatial resolution. The numerical error is given by

$$\|(h, hu, hv)\|_{\Delta x} = \Delta x \sum_i \left(c_0 \left|h_i - h^0_i\right| + \left|hu_i - hu^0_i\right| + \left|hv_i - hv^0_i\right|\right), \tag{A 21}$$

where $(h^0, hu^0, hv^0)$ corresponds to a reference run which was obtained with fine-grid Method 2 at $\Delta x/R_d = 0.0025$. (The reference solution may be as well obtained with any of the methods, provided the grid is sufficiently fine, see the convergence tests below.) Finally, $\|\cdot\|^q_{\Delta x}$ is the error in the potential vorticity as obtained from $(h, hu, hv)$:

$$\|(h, hu, hv)\|^q_{\Delta x} = \Delta x \sum_i \left|q_i - q^0_i\right|. \tag{A 22}$$

The effective spatial order is calculated as $n = (1/\log 2)\log((\|\cdot\|_{\Delta x})/(\|\cdot\|_{\Delta x/2}))$.

Tables 2–4 show that all three methods converge to the reference solution. Method 2 converges with a maximum effective spatial numerical order of 1.57. This is a standard

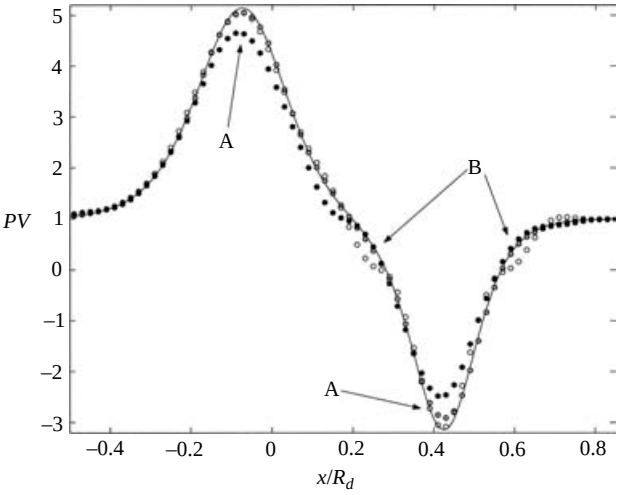


FIGURE 20. PV field at $t/T_f = 5.0$ as computed with three different methods. Method 1 (open circles) and Method 2 (grey dots) are described in Appendices A.1 and A.2, respectively; Method 3 (black dots) applies the Roe approximate Riemann solver with an operator splitting treatment of the source terms used by Kuo & Polvani (1997). The plain line is the reference run cited in Appendix A.3. The three methods are applied to the simulations of experiment (*a*) with $Ro = 1$, $Bu = 4$ (i.e. a configuration with shock formation, cf. figure 3 on a $\Delta x = 0.02R_d$ grid. The arrows A and B indicate the regions where the three solutions differ significantly at low resolution.

| $\Delta x/R_d$ | $\|\cdot\|_{\Delta x}$ | $\|\cdot\|^q_{\Delta x}$ | $n$ |
|---|---|---|---|
| 0.160 | 1.7736 | 2.4091 | 0.97 |
| 0.080 | 0.9076 | 2.0248 | 1.52 |
| 0.040 | 0.3171 | 0.5528 | 1.11 |
| 0.020 | 0.1467 | 0.2296 | 1.08 |
| 0.010 | 0.0695 | 0.1053 | 1.09 |
| 0.005 | 0.0326 | 0.0444 | – |

TABLE 2. Convergence table of Method 1 at $t/T_f = 5.0$ for experiment $a$ with $Bu = 4$ and $Ro = 1$. Both errors are computed between $x/R_d = -10$ and $x/R_d = 10$. The numerical spatial order is obtained as $n = (1/\log 2)\log((\|\cdot\|_{\Delta x})/(\|\cdot\|_{\Delta x/2}))$. The scale of $\|\cdot\|_{\Delta x}$ (resp. $\|\cdot\|^q_{\Delta x}$) is $gH^2/f$ (resp. $\sqrt{g/H}$).

| $\Delta x/R_d$ | $\|\cdot\|_{\Delta x}$ | $\|\cdot\|^q_{\Delta x}$ | $n$ |
|---|---|---|---|
| 0.160 | 0.3998 | 1.8043 | 1.51 |
| 0.080 | 0.1402 | 0.8898 | 1.21 |
| 0.040 | 0.0603 | 0.3779 | 1.16 |
| 0.020 | 0.0270 | 0.1522 | 1.22 |
| 0.010 | 0.0116 | 0.0636 | 1.57 |
| 0.005 | 0.0039 | 0.0219 | – |

TABLE 3. Same as table 2 but with Method 2.

value for second-order schemes in the presence of shocks. For more detailed accuracy testing see Audusse *et al.* (2004*b*). A good convergence is also obtained in the PV field. Method 3 converges moreslowly (order 1.04); this is due to its property of slow

| $\Delta x/R_d$ | $\|\cdot\|_{\Delta x}$ | $\|\cdot\|^q_{\Delta x}$ | $n$ |
|---|---|---|---|
| 0.160 | 0.7749 | 2.0888 | 0.82 |
| 0.080 | 0.4389 | 1.3662 | 0.97 |
| 0.040 | 0.2241 | 0.7156 | 1.01 |
| 0.020 | 0.1116 | 0.3525 | 1.01 |
| 0.010 | 0.0555 | 0.1687 | 1.04 |
| 0.005 | 0.0271 | 0.0784 | – |

TABLE 4. Same as table 2 but with Method 3.

| Experiment | Description | Parameters | Domain | Figure |
|---|---|---|---|---|
| *a* | Rossby adjustment | $Ro^a$, $Bu^a$ | Open | 2, 3, 4, 5, 8, 20 |
| *b* | Double-jet adjustment | $Ro^b$, $Bu^b$, $\alpha^b$ | Open | 6, 7 |
| *c* | Wave-perturbation of a jet | $Ro^c_{jet}$, $Bu^c_{jet}$, $Ro^c_p$, $Fr^c_p$ | Open | 9, 13, 14, 15 |
| *d* | Wave-perturbation of a double-jet | $Ro^d_{jet}$, $Bu^d_{jet}$, $\alpha^d$, $Ro^d_p$, $Fr^d_p$ | Open | 14, 15 |
| *e* | Nonlinear wave stability | $k^e$, $a^e$, $Ro^e_p$, $Fr^e_p$ | Periodic | 16, 17 |
| *f* | Harmonic wave adjustment | $Ro^f$, $Bu^f$ | Periodic | 18, 19 |

TABLE 5. Numerical experiments.

erosion of the PV-extrema (figure 20, arrow A). Method 1 also converges slower owing to the regions indicated by arrows B in figure 20. This property is more pronounced for strongly unbalanced $(h, hu, hv)$ (i.e. in the early stages of adjustment) and may be cured by using different treatment of the source-terms depending on the balance of the solution. It should be noted that the rapid convergence toward the correct solution observed with Method 2 is partially due to the second-order time-stepping scheme used in that case whereas only a first-order scheme is implemented in Method 1 and Method 3.

This comparison clearly reveals the advantages of Method 2, which we used.

## Appendix B. Relevant parameters and initial conditions of numerical experiments

In this section, we settle initial conditions and give relevant parameters for each of our numerical experiments. The experiments are summarized in table 5.

*Experiment a. Rossby adjustment*

Initial state:

$$\left.\begin{aligned} h(x,0) &= H, \\ u(x,0) &= 0, \\ v(x,0) &= VN_L(x), \end{aligned}\right\} \tag{B 1}$$

Parameters:

$$Ro^a = \frac{V}{fL}, \quad Bu^a = \frac{gH}{f^2L^2}. \tag{B 2}$$

*Experiment b. Double-jet adjustment*

Initial state:

$$\left.\begin{aligned} &h(x,0) = H, \\ &u(x,0) = 0, \\ &v(x,0) = V(N_L(x-\alpha^b) - N_L(x+\alpha^b)), \end{aligned}\right\} \tag{B 3}$$

Parameters:

$$Ro^b = \frac{V}{fL}, \quad Bu^b = \frac{gH}{f^2L^2}, \quad \alpha^b. \tag{B 4}$$

*Experiment c. Wave-perturbation of an adjusted jet*

Initial state:

$$\left.\begin{aligned} &h(x,0) = h^c(x), \\ &u(x,0) = u_p N_{L_p}(x), \\ &v(x,0) = V N_L(x), \end{aligned}\right\} \tag{B 5}$$

with

$$fv = g\frac{\mathrm{d}h^c}{\mathrm{d}x}, \quad h^c(0) = H.$$

Parameters:

$$Ro^c_{jet} = \frac{V}{fL}, \quad Bu^c_{jet} = \frac{gH}{f^2L^2}, \quad Ro^c_p = \frac{u_p}{fL_p}, \quad Fr^c_p = \frac{u_p}{\sqrt{gH}}. \tag{B 6}$$

*Experiment d. Wave-perturbation of an adjusted double-jet*

Initial state:

$$\left.\begin{aligned} &h(x,0) = h^d(x), \\ &u(x,0) = u_p N_{L_p}(x), \\ &v(x,0) = V(N_L(x-\alpha^d) - N_L(x+\alpha^d)), \end{aligned}\right\} \tag{B 7}$$

with

$$fv = g\frac{\mathrm{d}h^d}{\mathrm{d}x}, \quad h^d(\alpha^d) = H,$$

Parameters:

$$Ro^d_{jet} = \frac{V}{fL}, \quad Bu^d_{jet} = \frac{gH}{f^2L^2}, \quad Ro^d_p = \frac{u_p}{fL_p}, \quad Fr^d_p = \frac{u_p}{\sqrt{gH}}, \alpha^d. \tag{B 8}$$

*Experiment e. Perturbation of a nonlinear wave*

Initial state:

$$\left.\begin{aligned} &h(x,0) = h_w(x)\left(1 + \frac{u_p}{c}N_{L_p}(x)\right), \\ &u(x,0) = u_w(x), \\ &v(x,0) = v_w(x), \end{aligned}\right\} \tag{B 9}$$

with $(h_w, u_w, v_w)$ being the $L$-periodic exact nonlinear wave solution.

Parameters:

$$Ro^e = \frac{max|\boldsymbol{u}_w|}{fL}, \quad k^e = \frac{2\pi}{L}, \quad Ro^e_p = \frac{u_p}{fL_p}, \quad Fr^e_p = \frac{u_p}{c} \tag{B 10}$$

*Experiment f. Finite-amplitude harmonic wave adjustment*

Initial state:

$$\left.\begin{aligned} h(x,0) &= H\,(1 + a\,\sin(k^f x)) \\ u(x,0) &= a\frac{\hat{\omega}}{k^f}\,\sin(k^f x) \\ v(x,0) &= -a\frac{f}{k^f}\cos(k^f x) \end{aligned}\right\} \quad \text{with} \quad \hat{\omega} = \sqrt{c^2 k^{f\,2} + f^2}. \tag{B 11}$$

Parameters:

$$Ro^f = \frac{a\,c}{f\,L}, \quad k^f. \tag{B 12}$$

## REFERENCES


Audusse, E., Bouchut, F., Bristeau, M.-O., Klein, R. & Perthame, B. 2004*a* A fast and stable well-balanced scheme with hydrostatic reconstruction for shallow water flows. *SIAM J. Sci. Comput.* (to appear).

Audusse, E., Bristeau, M.-O. & Perthame, B. 2004*b* Second order kinetic scheme for saint-venant equations with source terms on unstructured grids. *Preprint INRIA*.

Bouchut, F. 2004 Nonlinear stability of finite volume methods for hyperbolic systems of conservation laws, and well-balanced schemes for sources. *Frontiers in Mathematics*. Birkhauser (to appear).

Houghton, D. D. 1969 Effect of rotation on the formation of hydraulic jumps. *J. Geophys. Res.* **74**, 1351–1360.

Kuo, A. C. & Polvani, L. M. 1997 Time-dependent fully nonlinear geostrophic adjustment. *J. Phys. Oceanogr.* **27**, 1614–1634.

Kuo, A. C. & Polvani, L. M. 1999 Wave–vortex interaction in rotating shallow water. Part 1. One space dimension. *J. Fluid Mech.* **394**, 1–27.

LeVeque, R. 1992 *Numerical Methods for Conservation Laws*. Birkhauser.

LeVeque, R. 1997 Wave-propagation algorithms for multidimensional hyperbolic systems. *J. Comput. Phys.* **131**, 327–353.

LeVeque, R. 1998 Balancing source terms and flux gradients in high-resolution Godunov methods: the quasi-steady wave-propagation algorithm. *J. Comput. Phys.* **146**, 346–365.

Lighthill, J. 1978 *Waves in Fluids*. Cambridge University Press.

Nof, D. 1984 Nonlinear internal waves in a rotating ocean. *J. Phys. Oceanogr.* **14**, 1683–1702.

Ostrovsky, L. 1978 Nonlinear internal waves in a rotating ocean. *Oceanology* **18**, 119–124.

Peregrine, D. 1998 Surf zone currents. *Theoret. Comput. Fluid Dyn.* **10**, 295–309.

Pratt, L. 1983 On inertial flow over topography. Part 1. Semigeostropic adjustment to an obstacle. *J. Fluid Mech.* **131**, 195–218.

Pratt, L. 1984 On inertial flow over topography. Part 2. Rotating channel flow near the critical speed. *J. Fluid Mech.* **145**, 95–110.

Rossby, C. 1938 On the mutual adjustment of pressure and velocity distributions in certain simple current systems II. *J. Mar. Res.* **1**, 239–263.

Rozhdestvenskii, B. & Yanenko, N. 1983 *Systems of Quasi-Linear Equations and their Applications to Gas Dynamics*. AMS.

Schar, C. & Smith, R. 1993 Shallow-water flow past an isolated topography. part 1: Vorticity production and wake formation. *J. Atmos. Sci.* **50**, 1373–1400.

Shrira, V. 1981 Propagation of nonlinear waves in a layer of rotating fluid. *Izv. Atmos. Ocean. Phys.* **17**, 55–59.

Shrira, V. 1986 On long strongly nonlinear waves in a rotating ocean. *Izv. Atmos. Ocean. Phys.* **22**, 298–305.

Whitham, G. B. 1974 *Linear and Nonlinear Waves*. Wiley.

Zeitlin, V., Medvedev, S. & Plougonven, R. 2003 Frontal geostrophic adjustment, slow manifold and nonlinear wave phenomena in one-dimensional rotating shallow water. Part 1. Theory. *J. Fluid Mech.* **481**, 269–290.